Draft version March 27, 2026
Typeset using LaTeX **twocolumn** style in AASTeX631

Revisiting the Claim for a Direct-Collapse Black Hole in UHZ1 at z = 10.05

Fan Zou [1], Elena Gallo [1], Zihao Zuo [1], Edmund Hodges-Kluck [2], Dieu D. Nguyen [1], Guido Roberts-Borsani [3], Piero Madau [4,5], Fabio Pacucci [6,7], Anil C. Seth [8] and Tommaso Treu [9]

[1] Department of Astronomy, University of Michigan, 1085 S University, Ann Arbor, MI 48109, USA
[2] X-ray Astrophysics Laboratory, NASA/GSFC, Greenbelt, MD 20771, USA
[3] Department of Physics & Astronomy, University College London, London, WC1E 6BT, UK
[4] Department of Astronomy & Astrophysics, University of California, 1156 High Street, Santa Cruz, CA 95064, USA
[5] Dipartimento di Fisica "G. Occhialini," Università degli Studi di Milano-Bicocca, Piazza della Scienza 3, I-20126 Milano, Italy
[6] Center for Astrophysics, Harvard & Smithsonian, 60 Garden St, Cambridge, MA 02138, USA
[7] Black Hole Initiative, Harvard University, 20 Garden St, Cambridge, MA 02138, USA
[8] Department of Physics and Astronomy, University of Utah, USA
[9] Physics and Astronomy Department, University of California, Los Angeles, CA 90095, USA

ABSTRACT

We reassess the direct collapse black hole (DCBH) interpretation of UHZ1 (UNCOVER-26185), a gravitationally lensed galaxy at $z_{\rm spec} = 10.054$. That interpretation rests on a hard (2–7 keV) X-ray excess detected with Chandra, attributed to a Compton-thick AGN with an inferred 2–10 keV luminosity of $L_{\rm X,int} \sim 10^{46}$ erg s^{-1} (Bogdán et al. 2024). The resulting extreme X-ray to rest-frame optical–IR ratio was taken as the hallmark signature of an "outsize black hole galaxy" at cosmic dawn. We analyse the full 2.2 Ms Chandra imaging dataset—including 0.95 Ms of unpublished observations—and present new JWST/MIRI photometry at $\lambda_{\rm obs} > 5$ μm. Across the full range of plausible Chandra data reductions, the 2–7 keV excess at the position of UHZ1 reaches a significance of only 2.3–2.9σ; the originally reported 4.2–4.4σ detection is sensitive to the specific astrometric alignment adopted and is not robustly reproducible. Moreover, the hard X-ray signal does not grow with the additional exposure, contrary to expectations for a steady source, indicating that any excess is not persistent. UHZ1 is also undetected in all nine MIRI imaging bands. Fitting red/obscured AGN SED templates to the tightest MIRI upper limit, we constrain the bolometric luminosity of any buried AGN to $L_{\rm bol} < 1.3 \times 10^{45}$ erg s^{-1}. These conclusions are further supported by independent JWST spectroscopy (Álvarez-Márquez et al. 2026), which reveals no AGN signatures in the rest-frame UV or optical. Taken together, the multiwavelength data paint a consistent picture of UHZ1 as a low-mass, metal-poor, star-forming galaxy in the early Universe, with no compelling evidence for a luminous obscured AGN, regardless of its proposed formation channel.

1. INTRODUCTION

The origin of supermassive black holes (SMBHs) is one of the most pressing unsolved problems at the intersection of high-energy astrophysics and galaxy formation. Over three hundred quasars powered by SMBHs with masses $M_{\rm BH} \gtrsim 10^9\ M_\odot$ have now been spectroscopically confirmed at $z \gtrsim 6$ (Fan et al. 2001, 2003; Mortlock et al. 2011; Wu et al. 2015; Bañados et al. 2018; Wang et al. 2021; Fan et al. 2023), implying that billion-solar-mass black holes were already in place less than one billion years after the Big Bang. Growing such objects from stellar-mass remnants ($M_{\rm seed} \sim 10$–$10^2\ M_\odot$) is challenging and, under standard radiatively efficient growth, requires nearly continuous Eddington-rate accretion for several hundred Myr (Madau & Rees 2001; Haiman 2004; Volonteri 2010; Inayoshi et al. 2020; Pacucci & Loeb 2022). This has motivated both theoretical work on more massive initial seeds (Rees 1984; Volonteri 2012; Natarajan 2014) and alternative rapid-growth scenarios for light seeds (Madau et al. 2014).

The most widely discussed alternative is the direct collapse scenario, in which primordial gas in atomic-cooling haloes ($T_{\rm vir} \gtrsim 10^4$ K) avoids fragmentation into stars when H_2 cooling is suppressed by a strong Lyman–Werner radiation field, and instead collapses to form a direct collapse black hole (DCBH) seed with $M_{\rm seed} \sim 10^4$–$10^6\ M_\odot$ (Bromm & Loeb 2003; Begelman et al. 2006; Lodato & Natarajan 2006; Begelman et al. 2008; Volonteri et al. 2008; Inayoshi et al. 2020). Starting from such a heavy seed would largely alleviate the timing problem, enabling growth to $\simeq 10^9\ M_\odot$ by $z \sim 6$ under more moderate accretion histories.

A key prediction of this scenario is that, during the rapid early growth phase, the BH mass can be comparable to or exceed the stellar mass of the host galaxy—the so-called "outsize black hole galaxy" (OBG; Natarajan et al. 2017; Scoggins et al. 2023; Scoggins & Haiman 2024) phase—in stark contrast to the $M_{\rm BH}/M_\star \sim 10^{-3}$ relation in the local Universe (Kormendy & Ho 2013). This extreme mass ratio manifests observationally as a very high ratio of rest-frame X-ray to optical flux: the accreting heavy seed dominates the bolometric output while the stellar mass of the host remains low, producing a source that is luminous in hard X-rays yet faint and red in the UV–optical (Pacucci et al. 2015, 2016; Natarajan et al. 2017). This distinctive multiwavelength signature is, in principle, what uniquely identifies a DCBH candidate at high redshift and distinguishes it from the more ordinary over-massive BHs increasingly reported at $z \sim 4$–7 by JWST (Pacucci et al. 2023; Harikane et al. 2023; Maiolino et al. 2024).

Against this backdrop, the discovery of UHZ1 (UNCOVER-26185) at $z \simeq 10.05$ was immediately recognized as potentially decisive. The source was first identified as a high-redshift candidate in deep NIRCam imaging of the Frontier Fields cluster Abell 2744 (Castellano et al. 2022, 2023; Bezanson et al. 2024). Its redshift was subsequently confirmed spectroscopically at $z_{\rm spec} = 10.054$ via JWST/NIRSpec Prism and JWST/MIRI LRS observations, which also yielded a stellar mass $M_\star = (1.7 \pm 0.3) \times 10^8\,M_\odot$ and a low metallicity $Z = (0.04 \pm 0.01)\,Z_\odot$ (Goulding et al. 2023; Álvarez-Márquez et al. 2026).

Gravitational lensing by Abell 2744 magnifies the source by a factor $\mu = 3.71^{+0.23}_{-0.23}$ (Bergamini et al. 2023), bringing it within reach of X-ray observation. Leveraging 1.25 Ms of archival Chandra/ACIS imaging of the Abell 2744 field, Bogdán et al. (2024) reported a 4.2–4.4 σ excess of hard X-ray counts (2–7 keV; rest-frame 22–88 keV) spatially coincident with UHZ1. The detection rests on only ~21 net counts above a background of ~21.4 counts, the latter dominated by the hot ($kT \sim 11$ keV) intra-cluster medium (ICM) of Abell 2744. The source is undetected in the soft band, consistent with extreme absorption. Spectral fitting with a Compton-thick AGN model (Yaqoob 2012) yielded a best-fit column density $N_{\rm H} \approx 8^{+\infty}_{-7} \times 10^{24}\,{\rm cm}^{-2}$, though the authors acknowledged severe degeneracy between $N_{\rm H}$ and L_X owing to the limited photon statistics. Adopting the lower 1σ bound on $N_{\rm H}$ and assuming the resulting bolometric luminosity to be Eddington-limited yields $M_{\rm BH} \sim 10^7$–$10^8\,M_\odot$, comparable to the host galaxy stellar mass (adopting instead the best-fit $N_{\rm H}$ would yield a black hole mass exceeding the entire host galaxy). The authors therefore interpreted UHZ1 as the first observational evidence for heavy-seed DCBH formation (Natarajan et al. 2024).

This interpretation rested on assumptions that were already sources of uncertainty at the time of publication. The published X-ray signal is below the 5σ threshold warranted for extraordinary claims—and the BH mass inference is the product of a long chain of model-dependent steps. The NIRSpec PRISM spectrum (Goulding et al. 2023) showed neither broad lines nor high-ionization UV emission, attributed to extreme obscuration, but the strongest rest-frame optical diagnostics (Hα, Hβ, [O III]) lay outside the NIRSpec wavelength coverage at $z \simeq 10$, preventing a direct test.

Independent confirmation was therefore urgently needed. The MIRI instrument on JWST provides a uniquely powerful diagnostic: at $z \simeq 10$, observed wavelengths $5 \lesssim \lambda_{\rm obs} \lesssim 25\,\mu$m sample the rest-frame 0.4–2.2 μm window, encompassing both the classical rest-optical emission lines used in AGN diagnostics (BPT; Baldwin et al. 1981; Kewley et al. 2001; Kauffmann et al. 2003) and the rest-frame ~1–2 μm near-IR continuum where thermal emission from a hot AGN torus becomes visible (Hickox & Alexander 2018; Lyu et al. 2022). This torus emission acts as a calorimeter for the buried AGN: regardless of the X-ray column density, an AGN with $L_{\rm bol} \sim 10^{45}\,{\rm erg\,s^{-1}}$ must heat its surrounding dust and reradiate a substantial fraction of that power in the near-IR, making mid-IR photometry a genuinely independent probe of the AGN hypothesis. Hot dusty tori have been directly detected with JWST/MIRI out to $z \sim 7$ (Bosman et al. 2024), demonstrating the feasibility of this approach.

Recent JWST observations have provided exactly these independent constraints. Álvarez-Márquez et al. (2026) presented deep (13.9 hr) JWST/MIRI LRS spectroscopy of UHZ1 as part of the PRImordial galaxy Survey with MIRI Spectroscopy (PRISMS; PID 8051), detecting Hβ+[O III]$\lambda\lambda$4960,5008 and Hα at 10σ and 8σ, respectively. The inferred nebular properties are inconsistent with a luminous obscured AGN: the UV-to-optical SED is well described by a low-dust stellar population with emission-line ratios placing the source in the low-metallicity star-forming locus of standard diagnostic diagrams, with no AGN ionizing continuum required. These results are consistent with an independent analysis by Fujimoto et al. (2024).

UHZ1 is therefore at the center of a growing multiwavelength tension with direct implications for the DCBH interpretation and, more broadly, for the reliability of X-ray–based BH mass estimates at cosmic dawn. In this paper we present a comprehensive reassessment using two new datasets. First, we reprocess the full Chandra dataset of Bogdán et al. (2024) and incorporate an additional 0.95 Ms of exposure obtained between 2023-05-24 and 2024-05-29, applying a homogeneous reduction and careful local treatment of the cluster background. Second, we present new JWST/MIRI imaging extending to $\lambda_{\rm obs} > 5\,\mu$m, providing the first direct constraints on the rest-frame near-IR continuum.

The remainder of this paper is structured as follows. The multiwavelength dataset is described in Section 2, where Section 2.1 presents the Chandra reanalyses, and Section 2.2 presents the MIRI imaging. Implications for the DCBH scenario are discussed in Section 3. Throughout we assume a flat ΛCDM cosmology with $H_0 = 67.7\,\mathrm{km\,s^{-1}\,Mpc^{-1}}$ and $\Omega_m = 0.310$ (Planck Collaboration et al. 2020).

2. OBSERVATIONS, DATA REDUCTION, AND ANALYSIS

2.1. *Chandra/ACIS*

We (re-)analyse the *Chandra*/ACIS imaging at the sky position of UHZ1 to independently assess the significance of the hard-band excess reported by Bogdán et al. (2024). Our approach proceeds in four steps: (*i*) homogeneous data reduction of both the original and extended datasets (Section 2.1.1); (*ii*) aperture photometry with careful treatment of the structured ICM background and a direct comparison with the published detection (Section 2.1.2); (*iii*) a Monte Carlo assessment of the sensitivity of the detection significance to astrometric registration choices (Section 2.1.3); and (*iv*) a temporal analysis of the hard-band signal across individual epochs to test the hypothesis of a steady source (Section 2.1.4).

2.1.1. *Observations and Data Reduction*

We consider two datasets: the same 1.25 Ms observations used by Bogdán et al. (2024) (hereafter the "B24 subset") and an extended 2.2 Ms dataset that also includes 0.95 Ms of new observations obtained between 2023 May and 2024 May (PI: A. Bogdán). Table 2.1 reports the utilized Chandra observations. The data were reduced with `CIAO` 4.18 and `CALDB` 4.12.3.

We first run the `chandra_repro` script with the option `check_vf_pha = yes` because all the observations were taken in the Very Faint mode. We then conduct the first-pass merging of these observations with `merge_obs` and use `wavdetect` to detect sources on the merged data between 0.5 − 7 keV with a "$\sqrt{2}$ sequence" of wavelet scales (1, 1.414, 2, 2.828, 4, 5.656, and 8 pixels) and a significance threshold of 10^{-6}. To assess any likely background flares, we then generate a source-free region by masking these detected source regions, where their sizes are enlarged by a factor of 2 and floored at 3″, as well as the central 5′ radius of Abell 2744. We then use `deflare` to clean background flares in each observations, leading to a 3.4% reduction of the effective exposure time. This cleaning procedure generally has negligible effects. When only analyzing the B24 subset, we do not apply the deflare procedure to be consistent with Bogdán et al. (2024).

A key systematic in this analysis is the relative astrometric alignment of individual observations, which becomes important for a marginal detection in a structured background. We therefore test three astrometry correction methods before performing the final merge:

1. No astrometry corrections.
2. Same as Bogdán et al. (2024), registration to reference X-ray sources detected in the single longest Chandra observation, i.e., ObsID = 8477 when analyzing the B24 subset or ObsID = 25926 when analyzing all the data.
3. Registration to reference optical sources in the Legacy Survey DR10 (Dey et al. 2019). To construct this reference list, we rely on the detected X-ray sources on the first-pass merged data and select bright sources with ≥ 50 net counts and PSF sizes ≤ 2.5″. These sources are then matched with the optical catalog with a matching radius of 1″, and the matched optical positions are used as the reference list.

When applicable, we use `fine_astro` to apply astrometric corrections to the cleaned observations before performing a final merge. The impact of the above choices on the detection significance is quantified in Sections 2.1.2 and 2.1.3.

2.1.2. *Aperture Photometry and Detection Significance*

With the reduced and merged event files in hand, we perform aperture photometry on the hard (2–7 keV), soft (0.5–2 keV), and full (0.5–7 keV) bands, following the exact aperture configuration of Bogdán et al. (2024) to enable a direct comparison. Specifically, we adopt a circular source aperture of radius $r_{\rm src} = 1''$ and a local background annulus with radii $r_{\rm in} = 3''$ and $r_{\rm out} = 6''$ (area ratio $A_{\rm bkg}/A_{\rm src} = 27$), both centered at R.A. = 00:14:16.096 and Dec. = −30:22:40.285.

Because UHZ1 lies in projection near the core of Abell 2744, the local background is dominated by the hot ($kT \sim 11$ keV) ICM and is substantially elevated relative to a blank field. Spatial variations in the ICM surface brightness on arcsecond scales could in principle bias the local background estimate, so we perform an independent check. We model the 1′ × 1′ region around UHZ1 (masking any detected point sources in addition to the UHZ1 aperture) with a 4th-order polynomial in detector coordinates using Poisson statistics. The resulting expected background in the $r_{\rm src} = 1''$ aperture is consistent with the annular estimate for the same merged dataset at a $\lesssim 0.1$ count level, indicating that the mean local background level is not strongly method-dependent for this test. Similar conclusions were also drawn by Bogdán et al. (2024). Nevertheless, sub-arcsecond variations in the ICM surface brightness cannot be fully excluded, as they approach the Chandra pixel scale.

We quantify the detection significance via the binomial no-source probability P_B (Weisskopf et al. 2007), which is better suited than a simple signal-to-noise ratio for the low-count

Table 1. Chandra observations of the field of view of UHZ1 (Abell 2744)

ObsID (1)	Date (2)	T_{exp} (3)	$T_{\mathrm{exp}}^{\mathrm{clean}}$ (4)	ObsID (1)	Date (2)	T_{exp} (3)	$T_{\mathrm{exp}}^{\mathrm{clean}}$ (4)	ObsID (1)	Date (2)	T_{exp} (3)	$T_{\mathrm{exp}}^{\mathrm{clean}}$ (4)
2212	2001-09-03	24.8	24.1	25934	2022-04-21	19.3	19.2	25969	2022-10-09	27.7	27.2
7712	2007-09-10	8.1	8.1	25935	2023-08-20	24.1	22.5	25970	2022-06-12	24.8	24.2
7915	2006-11-08	18.6	18.6	25936	2023-01-26	12.9	12.9	25971	2022-05-04	12.6	12.4
8477	2007-06-10	45.9	45.7	25937	2022-11-27	30.8	30.2	25972	2022-05-18	31.7	31.7
8557	2007-06-14	27.8	27.8	25938	2022-11-26	18.7	18.1	25973	2022-11-11	18.1	17.4
25277	2023-10-02	18.7	18.2	25939	2023-01-28	14.3	13.4	26280	2022-01-18	11.7	11.5
25278	2022-12-02	9.8	9.8	25940	2023-08-10	27.7	27.2	27347	2022-09-09	22.0	20.7
25279	2022-09-06	24.5	23.4	25941	2023-06-09	32.6	31.4	27449	2022-09-24	9.8	9.8
25907	2022-11-08	36.8	36.5	25942	2022-05-04	15.2	14.4	27450	2022-09-26	9.8	9.8
25908	2022-09-23	22.6	21.2	25943	2023-08-31	16.7	16.2	27556	2022-11-15	25.2	24.4
25909	2023-05-24	19.3	18.8	25944	2022-09-08	21.6	21.1	27563	2023-06-08	11.7	10.9
25910	2022-09-25	19.3	19.2	25945	2022-09-27	17.0	16.8	27575	2022-12-02	19.7	19.7
25911	2022-04-19	16.9	15.8	25946	2023-07-01	29.7	29.1	27678	2023-01-27	12.4	12.4
25912	2022-04-18	15.4	15.1	25947	2023-09-24	14.9	13.6	27679	2023-01-28	11.9	7.1
25913	2022-09-03	19.6	19.6	25948	2022-09-30	27.9	27.3	27680	2023-01-28	13.2	12.4
25914	2022-10-15	28.2	27.0	25949	2023-10-27	20.8	20.2	27681	2023-01-29	9.8	9.2
25915	2022-09-03	21.1	20.3	25950	2023-06-30	29.7	28.9	27739	2023-10-01	21.3	20.8
25916	2023-09-03	22.2	21.7	25951	2022-11-18	28.7	27.9	27780	2023-08-21	14.9	14.2
25917	2023-06-22	35.6	33.8	25952	2023-09-27	10.8	9.8	27856	2023-05-25	15.9	15.2
25918	2022-09-13	20.6	20.6	25953	2022-09-17	24.8	24.2	27857	2023-05-26	12.9	12.7
25919	2022-06-13	25.3	24.8	25954	2022-04-24	13.4	13.4	27896	2023-06-10	13.7	13.7
25920	2022-06-13	30.5	29.9	25955	2023-07-20	43.4	40.4	27974	2023-08-05	28.7	26.9
25921	2023-08-04	16.9	16.9	25956	2022-09-02	13.9	13.6	28370	2023-08-13	20.7	19.7
25922	2022-06-14	31.4	30.9	25957	2022-09-08	21.8	21.5	28483	2023-08-19	20.2	18.4
25923	2022-09-04	10.9	10.4	25958	2022-05-04	12.3	12.1	28872	2023-09-01	13.1	12.1
25924	2022-09-07	21.8	21.5	25959	2023-08-05	15.4	15.1	28886	2023-09-10	10.0	9.3
25925	2022-09-02	23.6	23.2	25960	2023-07-08	24.8	23.2	28887	2023-09-10	19.8	19.1
25926	2023-07-12	61.2	59.9	25961	2023-09-09	18.8	18.2	28910	2023-10-25	25.8	24.7
25927	2023-09-16	20.5	19.4	25962	2023-09-11	21.8	21.3	28920	2023-09-25	15.3	14.5
25928	2022-05-03	15.9	15.6	25963	2022-11-26	37.6	35.7	28934	2023-09-29	19.8	18.8
25929	2022-08-26	27.7	26.4	25964	2023-09-05	20.3	19.0	28951	2023-10-05	12.9	12.1
25930	2022-11-15	19.9	19.7	25965	2023-07-07	35.7	34.1	28952	2023-10-08	13.8	13.5
25931	2022-04-23	14.6	14.3	25966	2023-08-13	18.8	18.6	29207	2024-05-29	19.7	15.2
25932	2022-05-05	14.1	14.1	25967	2022-08-01	33.6	33.1	29427	2024-05-29	18.7	17.4
25933	2023-08-15	23.9	23.1	25968	2022-07-12	27.5	26.7	**Total**	—	**2200.6**	**2125.0**

Notes. Columns are: (1) Chandra observation ID, in ascending order; (2) observation start date; (3) total exposure time in ks; (4) cleaned exposure time in ks. The first observation (ObsID = 2212) was carried out with ACIS-S; all remaining observations were conducted with ACIS-I.

regime encountered here. We calculate:

$$P_B = \sum_{X=S}^{N} \frac{N!}{X!(N-X)!} p^X (1-p)^{N-X} = I_\beta(p, S, N-S+1), \quad (1)$$

where S is the number of counts in the source region, N is the number of total counts in both the source and background regions, $p = A_{\mathrm{src}}/(A_{\mathrm{src}} + A_{\mathrm{bkg}})$, and I_β is the regularized incomplete Beta function, which is useful for better numerical stability here. P_B is then converted to a nominal Gaussian significance level.

The results for all dataset and astrometry choices are summarized in Table 2. *Across all cases, we find only a marginal signal in the hard band at the* 2.3–2.9σ *level, substantially less significant than the* 4.2–4.4σ *reported by Bogdán et al.*

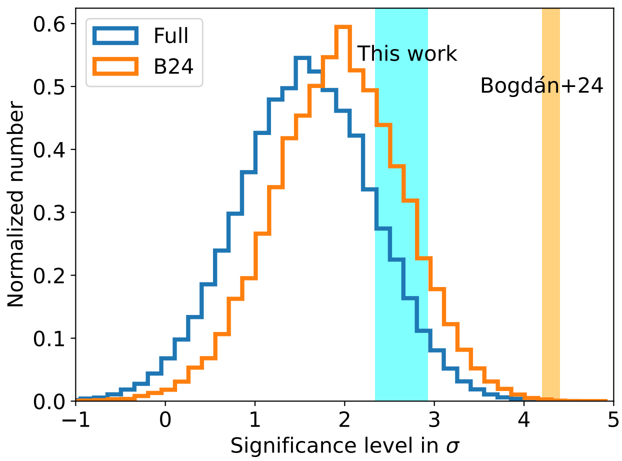

Figure 1. Distribution of hard-band detection significance obtained by randomly shifting the astrometric registration of each observation. Both histograms are normalized to unit sum. Blue and orange histograms correspond to the full 2.2 Ms dataset and the B24 subset (Bogdán et al. 2024), respectively. The cyan shaded band marks the range of detection significances measured in this work (Table 2); the orange shaded band marks the significance reported by Bogdán et al. (2024). The 4.2–4.4σ value of Bogdán et al. (2024) is recovered in fewer than 0.1% of Monte Carlo realizations, demonstrating its sensitivity to the assumed astrometric alignment.

(2024). The soft band is fully undetected, and the full-band significance reaches only 1.1–2.1σ.

2.1.3. *Sensitivity to Astrometric Registration*

The discrepancy between the hard-band significance reported above and the value reported by Bogdán et al. (2024) motivates a quantitative assessment of how sensitive a marginal detection in this field is to sub-arcsecond astrometric registration choices. We experiment by randomly shifting each observation. The shifting offsets are generated independently from a Gaussian distribution with a 0.5″ dispersion along both the R.A. and Dec. directions, and thus the absolute offset would follow a Rayleigh distribution with a 68% quantile of 0.8″ and a 90% quantile of 1.1″, consistent with the expected Chandra absolute astrometric accuracy.[1] We conduct this random shifting 10^5 times and plot the distribution of the resulting detection significance in Figure 1.

The broad distribution in Figure 1 demonstrates that *astrometric uncertainties alone can introduce or suppress apparent excesses of up to* 3–4σ *at this source position*. The reported 4.2–4.4σ of Bogdán et al. (2024) resides in the extreme tail of the distribution, with only 0.04% (0.01%) of the B24 (full) random-shifting results reaching 4.2σ. This suggests that the original detection is sensitive to a particularly favorable astrometric alignment, and that the significance is not robustly recovered across the full range of plausible reductions of the same data.

2.1.4. *Temporal Behavior of the Hard-Band Signal*

A genuine steady X-ray source should produce net counts that grow proportionally with exposure time. We use the extended 2.2 Ms dataset to test whether the hard-band signal at the UHZ1 position is consistent with a steady source. When the dataset is extended from the 1.25 Ms B24 subset to a total exposure of 2.2 Ms, the inferred net counts *do not increase in proportion to exposure time*, and their source signal significance remains similarly marginal in Table 2.

To examine this behavior across individual epochs, Figure 2 shows the hard-band net count rate in the 1″ source aperture for each individual observation. The binned light curve constructed from individual observations shows a positive net count rate in earlier epochs, but the net rate is consistent with zero in the more recent 0.95 Ms observations, although this difference is not statistically sufficient to claim variability. Nevertheless, the failure of the signal to accumulate as expected for a steady source further undermines the case for a robust detection.

2.2. *JWST/MIRI Imaging*

We analyze JWST/MIRI imaging observations of UHZ1 obtained as part of PID 6123 (PIs: E. Gallo & G. Roberts-Borsani). The data span the full suite of nine MIRI broadband filters, from F560W to F2550W, providing continuous coverage of the observed-frame mid-infrared between 5.6 and 25.5 μm, corresponding to rest-frame wavelengths of approximately 0.5–2.3 μm at the redshift of UHZ1.

We retrieve the stage 3 mosaics (`_i2d.fits`) from the Mikulski Archive for Space Telescopes (MAST). We mask detected sources and then estimate the background map using `photutils` (Bradley et al. 2025), with a 3σ clipping threshold to exclude potential sources. Visual inspection of each background-subtracted mosaic at the known position of UHZ1 reveals no source above the local noise level in any of the nine filters.

To quantify the significance of the non-detections, we extract the flux within a circular aperture enclosing 50% of the PSF energy in each band, centered on the UHZ1 position. The local background RMS noise is estimated as the standard deviation of fluxes measured in apertures of identical radius, placed randomly in nearby source-free regions. The signal-to-noise ratio is consistent with zero in all nine bands, confirming that UHZ1 is undetected across all MIRI imaging filters. A variance-weighted stack of all nine background-subtracted mosaics likewise yields a non-detection.

The resulting 3σ upper limits on the mid-infrared flux density of UHZ1 are listed in Table 3 and are used in Section 3 to place upper limits on the luminosity of any buried AGN.

[1] https://cxc.cfa.harvard.edu/cal/ASPECT/celmon/

Table 2. Detection Significance Summary

Data	Soft band			Hard band			Full band		
	$C_{\rm tot}$	$C_{\rm net}$	Significance	$C_{\rm tot}$	$C_{\rm net}$	Significance	$C_{\rm tot}$	$C_{\rm net}$	Significance
(1)	(2)	(3)	(4)	(2)	(3)	(4)	(2)	(3)	(4)
Bogdán et al. (2024)				42	21.4	$4.2-4.4\sigma$			
B24 (1)	19	−1.4	-0.4σ	34	14.5	2.8σ	53	13.1	1.9σ
B24 (2)	20	−0.6	-0.2σ	35	15.1	2.9σ	55	14.6	2.1σ
B24 (3)	16	−4.6	-1.1σ	32	12.4	2.4σ	48	7.8	1.1σ
Full (1)	34	1.8	0.2σ	54	19.1	2.9σ	88	20.9	2.3σ
Full (2)	29	−1.5	-0.3σ	49	15.1	2.3σ	78	13.6	1.6σ
Full (3)	27	−4.1	-0.8σ	50	15.7	2.4σ	77	11.6	1.3σ

Notes. (1) Merged dataset used. The first row reproduces the values reported in Bogdán et al. (2024). "B24" and "Full" denote the 1.25 Ms B24 subset and the 2.2 Ms full dataset, respectively; the number in parentheses indicates the astrometry correction method applied (see Section 2.1.1). (2) Total counts within the 1″ source aperture. (3) Net counts within the 1″ source aperture. (4) Detection significance.

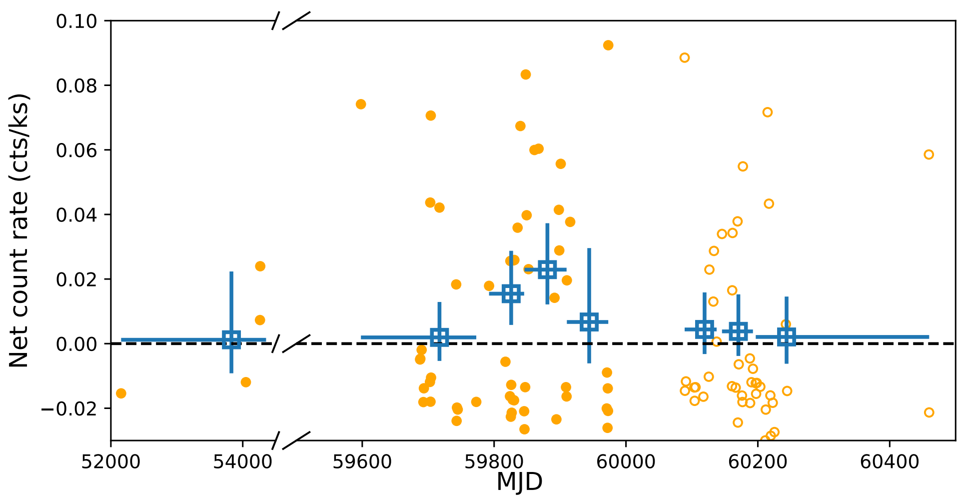

Figure 2. Hard-band net count rates in the 1″ source aperture. Each orange point stands for one observation, where the filled (open) ones represent those in (not in) the B24 subset. The open squares are binned to reach ≈ 100 – 300 ks. Their abscissa error bars represent the timespan of the corresponding bin, and their ordinate error bars reflect 1σ source-region count uncertainties calculated based on Gehrels (1986). The net count rate is consistent with zero in the more recent 0.95 Ms observations.

3. DISCUSSION

We present a reassessment of the evidence for a luminous, heavily obscured AGN in UHZ1 at z≃10.05, combining a reanalysis of the full 2.2 Ms Chandra dataset with new JWST/MIRI photometric limits on the mid-infrared continuum. Our principal conclusion is that no compelling evidence for such an AGN exists. The case for one rests on a hard X-ray excess that, under closer scrutiny, proves to be of marginal statistical significance. Our reanalysis of the same 1.25 Ms Chandra dataset used by Bogdán et al. (2024), and of the extended 2.2 Ms dataset incorporating all available observations through 2024 May, fails to reproduce a robust detection. Across reasonable, reproducible reductions of the 2–7 keV data, the inferred detection significance at the UHZ1 position spans ∼ 2.3–2.9σ and is sensitive to sub-arcsecond astrometric registration (Table 2; Section 2.1.2). The Monte Carlo astrometric analysis (Section 2.1.3) shows that the 4.2–4.4σ reported by Bogdán et al. (2024) lies in the extreme tail of the distribution of outcomes achievable under plausible registration choices, with only 0.04% of random realizations reaching that significance. Moreover, when the dataset is extended from 1.25 Ms to 2.2 Ms, the hard-band net counts do not grow in proportion to the added exposure time: the 0.95 Ms of new observations contribute negligible additional signals (Section 2.1.4), behavior that is inconsistent with a steady point source. Taken together, the evidence for a point-like X-ray counterpart to UHZ1 is not statistically

Table 3. JWST/MIRI photometric results

Band	Pivot wavelength	Exposure time	Flux
	(μm)	(seconds)	(μJy)
(1)	(2)	(3)	(4)
F560W	5.64	6649	< 0.13
F770W	7.64	3519	< 0.23
F1000W	9.95	1987	< 0.36
F1130W	11.31	4163	< 0.56
F1280W	12.81	2231	< 0.66
F1500W	15.06	1010	< 1.14
F1800W	17.98	1232	< 2.17
F2100W	20.80	2398	< 6.07
F2550W	25.36	5483	< 26.23

Notes. (1) JWST/MIRI imaging filter used for the observations. (2) Pivot wavelength of the broadband filter. (3) Total on-source exposure time for each filter. The exposure times vary among filters because the observations were optimized to achieve comparable sensitivity limits given the wavelength-dependent background and detector performance of MIRI. (4) Measured 3σ flux density upper limits derived from aperture photometry at the galaxy center after background subtraction.

robust.

The SED of UHZ1 is shown in Figure 3, with data from JWST/NIRCam (Suess et al. 2024), JWST/MIRI LRS continuum (Álvarez-Márquez et al. 2026), and the MIRI photometric limits derived in this work (Section 2.2). Independent of the X-ray analysis, the JWST/MIRI photometry at $\lambda_{\rm obs} > 8\ \mu$m (Section 2.2) yields an upper limit to the bolometric luminosity of any AGN that may be buried within UHZ1. To quantify this limit, we consider two AGN SED templates: (*i*) the "Torus" template of Polletta et al. (2006), and (*ii*) the extremely red SED of hot dust-obscured galaxies (Hot DOGs; Fan et al. 2016). The former is for typical heavily obscured quasars, while the latter represents the most conservative benchmark case because Hot DOGs are among the reddest, most infrared-luminous galaxies known at $z \lesssim 4$ and are powered by deeply buried, rapidly accreting AGN. We restrict the template fits to rest-frame wavelengths > 1 μm (i.e., observed-frame > 11 μm), since shorter-wavelength emission is (*i*) more susceptible to host-galaxy obscuration,[2] and (*ii*) subject to either a highly uncertain leaking fraction of intrinsic optical light or non-negligible host-galaxy contamination. Each template is scaled upward until it reaches the tightest MIRI constraint: F1500W for the Torus template and F1800W for the Hot DOG template, as shown in Figure 3.

[2] Nevertheless, the host galaxy of UHZ1 has only little obscuration, with an SED-based best-fit $A_V = 0.2$ mag (Álvarez-Márquez et al. 2026).

Both templates are dominated by hot dust emission. If instead the obscuring gas in UHZ1 were dust-free—plausible in the early Universe—no IR dust emission would be expected. In that case, however, the rest-frame UV-to-optical AGN SED would remain visible (e.g., Natarajan et al. 2024; Pacucci et al. 2026), and the NIRCam data in Figure 3 would impose considerably stronger constraints. The upper limits derived from the MIRI non-detections under the hot-dust assumption are therefore conservative.

After correcting for a gravitational magnification factor of $3.71^{+0.23}_{-0.23}$ (Bergamini et al. 2023), the MIRI non-detections constrain the bolometric luminosity of any buried AGN. For the Torus template we obtain $L_{\rm bol} < 1.3 \times 10^{45}$ erg s^{-1}. Applying the same 2–10 keV bolometric correction as Bogdán et al. (2024) ($L_{\rm bol}/L_{\rm X,int} = 21$–73), this limit translates into an upper bound to the intrinsic X-ray luminosity of $L_{\rm X,int} <$ (1.8–6.2) $\times\ 10^{43}$ erg s^{-1}. For the Hot DOG template, the far-infrared emission may carry a non-negligible contribution from host starburst activity (Tsai et al. 2015), making a clean bolometric inference unreliable. Separately, we use both templates to constrain the rest-frame 6 μm AGN luminosity, $L_{6\mu{\rm m}}$, which is tightly correlated with $L_{\rm X}$ and largely free from host contamination. We obtain $L_{6\ \mu{\rm m}} < 3.1 \times 10^{44}$ erg s^{-1} and $L_{6\ \mu{\rm m}} < 3.0 \times 10^{45}$ erg s^{-1} for the Torus and Hot DOG templates, respectively. Using the $L_{6\mu{\rm m}}$–$L_{\rm X,int}$ relation of Stern (2015), these yield $L_{\rm X,int} < 9.6 \times 10^{43}$ and $< 4.2 \times 10^{44}$ erg s^{-1}, respectively. Combining all $L_{\rm bol}$- and $L_{6\mu{\rm m}}$-based constraints, the MIRI data limit the intrinsic X-ray luminosity of any buried AGN in UHZ1 to $L_{\rm X,int} <$ (1.8–42) $\times\ 10^{43}$ erg s^{-1}—one to two orders of magnitude below the value inferred by Bogdán et al. (2024) under a Compton-thick model ($L_{\rm X,int} = 9 \times 10^{45}$ erg s^{-1}, $N_{\rm H} = 8^{+\infty}_{-7} \times 10^{24}$ cm^{-2}), itself uncertain given the low significance of the X-ray detection reported in our reanalysis.

The X-ray and mid-IR results presented here are corroborated by a consistent body of evidence from independent JWST observations, which we summarize for completeness. In each case, the data disfavor the presence of a luminous obscured AGN:

1. *Absence of AGN-like spectral features in the rest-UV (Goulding et al. 2023):* the NIRSpec spectrum lacks the prominent high-ionization UV lines typically associated with accreting sources at high redshift (e.g., strong C IV, N V, He II), in contrast to confirmed $z \gtrsim 9$ systems with comparable claimed X-ray luminosities (Kovács et al. 2024; Napolitano et al. 2025).

2. *Low-excitation rest-optical nebular spectrum (Álvarez-Márquez et al. 2026):* MIRI/LRS detects Hβ+[O III] and Hα with unusually low excitation compared to both star-forming and AGN samples at $z \gtrsim 3$.

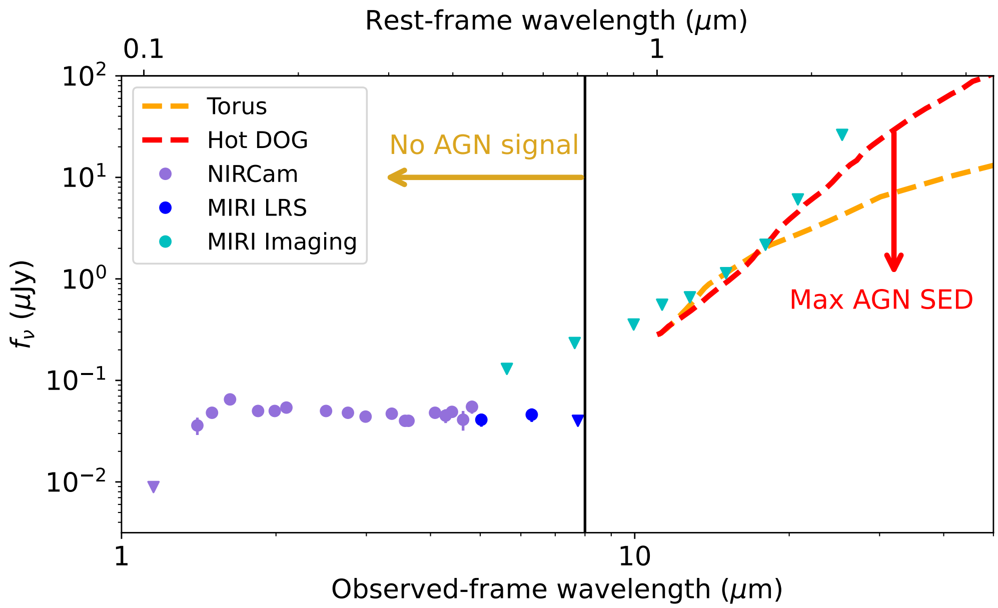

Figure 3. Observed SED of UHZ1. Filled circles are photometric detections and downward triangles are 3σ upper limits. The vertical black line marks $\lambda_{\rm obs} = 8\ \mu$m (rest-frame $\sim 0.7\ \mu$m), separating the NIRCam and MIRI LRS from the redder MIRI imaging bands. At $\lambda_{\rm obs} < 8\ \mu$m, the SED is fully consistent with an unobscured, low-mass, metal-poor, star-forming galaxy with no AGN contribution. At $\lambda_{\rm obs} > 8\ \mu$m, the MIRI non-detections place a direct upper bound on the bolometric luminosity of any buried AGN. The dashed orange and red curves show the maximally allowed normalization of the Torus (Polletta et al. 2006) and Hot DOG (Fan et al. 2016) AGN SED templates, respectively, each scaled to the F1500W and F1800W upper limits in Table 3. The bolometric luminosity implied by these upper envelopes falls one to two orders of magnitude below the intrinsic X-ray luminosity inferred by Bogdán et al. (2024) under a Compton-thick model, ruling out a luminous buried AGN of that magnitude in UHZ1.

The inferred ionization parameter ($\log U \simeq -2.5$) and optical diagnostic ratios occupy the locus of low-metallicity stellar photoionization models rather than AGN grids.

3. *No evidence for the large dust obscuration required by a Compton-thick interpretation (Algera et al. 2025; Álvarez-Márquez et al. 2026):* Balmer decrements are consistent with Case B recombination ($A_V \lesssim 0.4$ mag). Deep ALMA non-detections independently constrain the cold dust mass to $M_{\rm dust} \lesssim 5.5 \times 10^5\ M_\odot$, providing little support for a dust-rich host capable of hiding a luminous nucleus.

4. *Tension between recombination-line luminosity and claimed X-ray power (Álvarez-Márquez et al. 2026):* standard $L_{\rm H\alpha}$–L_X scalings predict $L_{2-10\,\rm keV} \sim$ few $\times\ 10^{43}$ erg s^{-1} from the observed Hα luminosity, at least an order of magnitude below the Compton-thick X-ray inference, with the absence of high-excitation narrow lines further weakening the type 2 AGN hypothesis.

These results have direct implications for the interpretation of UHZ1 as a direct collapse black hole candidate. The high black hole mass ($\sim 10^7$–$10^8\ M_\odot$) inferred from the X-ray signal by Bogdán et al. (2024) was taken to imply a DCBH seed, given the limited time available for black hole growth at $z \simeq 10$. The DCBH scenario further requires an outsize black hole—with $M_{\rm BH}$ comparable to or exceeding $M_\star$—that dominates the bolometric output, producing a source luminous in hard X-rays yet faint in the rest-frame UV–optical (Natarajan et al. 2017; Pacucci et al. 2023). The marginal significance of the X-ray detection undermines the claim of a luminous buried AGN; the mid-IR SED places a stringent upper bound on any such luminosity; the rest-frame UV–optical is consistent with stellar photoionization at low metallicity; and the dust content is insufficient to support the Compton-thick column density required by the Bogdán et al. (2024) spectral model. None of the multiwavelength criteria expected of a DCBH candidate are satisfied *beyond reasonable doubt*. More broadly, this case illustrates the risks of inferring BH masses from marginal X-ray detections in cluster fields where the ICM provides a bright, spatially structured background. The long inference chain from raw counts to $M_{\rm BH} \sim 10^7$–$10^8\ M_\odot$ can propagate and amplify systematic errors to produce apparently compelling results that do not survive independent scrutiny.

Given that the claim of a DCBH seed at $z \simeq 10$ is extraordinary, the burden of proof is correspondingly high. A comprehensive reanalysis of all available 2.2 Ms Chandra data, combined with new JWST/MIRI photometric limits and existing JWST spectroscopy, finds no compelling evidence for a luminous, obscured AGN in UHZ1 at $z \simeq 10.05$. The multi-wavelength data are consistent with UHZ1 being a low-mass ($M_\star \sim 10^8\,M_\odot$), metal-poor ($Z \sim 0.04\,Z_\odot$), star-forming (SFR $\sim 1\,M_\odot\,\mathrm{yr}^{-1}$) galaxy.

REFERENCES

Algera, H. S. B., Inami, H., Oesch, P. A., et al. 2025, ApJL, 978, L5

Álvarez-Márquez, J., Colina, L., Crespo-Gomez, A., et al. 2026, arXiv e-prints, arXiv:2602.02323

Bañados, E., Venemans, B. P., Mazzucchelli, C., et al. 2018, Nature, 553, 473

Baldwin, J. A., Phillips, M. M., & Terlevich, R. 1981, PASP, 93, 5

Begelman, M. C., Rossi, E. M., & Armitage, P. J. 2008, MNRAS, 387, 1649

Begelman, M. C., Volonteri, M., & Rees, M. J. 2006, MNRAS, 370, 289

Bergamini, P., Acebron, A., Grillo, C., et al. 2023, ApJ, 952, 84

Bezanson, R., Labbe, I., Whitaker, K. E., et al. 2024, ApJ, 974, 92

Bogdán, Á., Goulding, A. D., Natarajan, P., et al. 2024, Nature Astronomy, 8, 126

Bosman, S. E. I., Kakiichi, K., Meyer, R. A., et al. 2024, ApJ, 961, 105

Bradley, L., Sipőcz, B., Robitaille, T., et al. 2025, astropy/photutils: 2.3.0, v2.3.0, Zenodo, doi:10.5281/zenodo.17129028. https://doi.org/10.5281/zenodo.17129028

Bromm, V., & Loeb, A. 2003, ApJ, 596, 34

Castellano, M., Fontana, A., Treu, T., et al. 2022, ApJL, 936, L14

—. 2023, ApJL, 943, L9

Dey, A., Schlegel, D. J., Lang, D., et al. 2019, AJ, 157, 168

Fan, L., Han, Y., Nikutta, R., Drouart, G., & Knudsen, K. K. 2016, ApJ, 823, 107

Fan, X., Bañados, E., & Simcoe, R. A. 2023, ARA&A, 61, 373

Fan, X., Narayanan, V. K., Lupton, R. H., et al. 2001, AJ, 122, 2833

Fan, X., Strauss, M. A., Schneider, D. P., et al. 2003, AJ, 125, 1649

Fujimoto, S., Arrabal Haro, P., Dickinson, M., et al. 2024, ApJ, 965, 108

Gehrels, N. 1986, ApJ, 303, 336

Goulding, A. D., Greene, J. E., Setton, D. J., et al. 2023, ApJL, 955, L24

Haiman, Z. 2004, ApJ, 613, 36

Harikane, Y., Zhang, Y., Nakajima, K., et al. 2023, ApJ, 955, 94

Hickox, R. C., & Alexander, D. M. 2018, ARA&A, 56, 625

Inayoshi, K., Visbal, E., & Haiman, Z. 2020, ARA&A, 58, 27

Kauffmann, G., Heckman, T. M., Tremonti, C., et al. 2003, MNRAS, 346, 1055

Kewley, L. J., Dopita, M. A., Sutherland, R. S., Heisler, C. A., & Trevena, J. 2001, ApJ, 556, 121

Kormendy, J., & Ho, L. C. 2013, ARA&A, 51, 511

Kovács, O. E., Bogdán, Á., Natarajan, P., Tremblay, G. R., & Goulding, A. D. 2024, ApJL, 965, L21

Lodato, G., & Natarajan, P. 2006, MNRAS, 371, 1813

Lyu, J., Alberts, S., Rieke, G. H., & Rujopakarn, W. 2022, ApJ, 941, 191

Madau, P., Haardt, F., & Dotti, M. 2014, ApJL, 784, L38

Madau, P., & Rees, M. J. 2001, ApJL, 551, L27

Maiolino, R., Scholtz, J., Witstok, J., et al. 2024, Nature, 627, 59

Mortlock, D. J., Warren, S. J., Venemans, B. P., et al. 2011, Nature, 474, 616

Napolitano, L., Castellano, M., Fontana, A., et al. 2025, ApJL, 979, L9

Natarajan, P. 2014, ApJL, 788, L1

Natarajan, P., Pacucci, F., Ferrara, A., et al. 2017, ApJ, 838, 117

Natarajan, P., Pacucci, F., Ricarte, A., et al. 2024, ApJL, 960, L1

Pacucci, F., Ferrara, A., Grazian, A., et al. 2016, MNRAS, 459, 1432

Pacucci, F., Ferrara, A., & Kocevski, D. D. 2026, arXiv e-prints, arXiv:2601.14368

Pacucci, F., Ferrara, A., Volonteri, M., & Dubus, G. 2015, MNRAS, 454, 3771

Pacucci, F., & Loeb, A. 2022, MNRAS, 509, 1885

Pacucci, F., Nguyen, B., Carniani, S., Maiolino, R., & Fan, X. 2023, ApJL, 957, L3

Planck Collaboration, Aghanim, N., Akrami, Y., et al. 2020, A&A, 641, A6

Polletta, M. d. C., Wilkes, B. J., Siana, B., et al. 2006, ApJ, 642, 673

Rees, M. J. 1984, ARA&A, 22, 471

Scoggins, M. T., & Haiman, Z. 2024, MNRAS, 531, 4584

Scoggins, M. T., Haiman, Z., & Wise, J. H. 2023, MNRAS, 519, 2155

Stern, D. 2015, ApJ, 807, 129

Suess, K. A., Weaver, J. R., Price, S. H., et al. 2024, ApJ, 976, 101

Tsai, C.-W., Eisenhardt, P. R. M., Wu, J., et al. 2015, ApJ, 805, 90

Volonteri, M. 2010, A&A Rv, 18, 279

—. 2012, Science, 337, 544

Volonteri, M., Lodato, G., & Natarajan, P. 2008, MNRAS, 383, 1079

Wang, F., Yang, J., Fan, X., et al. 2021, ApJL, 907, L1

Weisskopf, M. C., Wu, K., Trimble, V., et al. 2007, ApJ, 657, 1026

Wu, X.-B., Wang, F., Fan, X., et al. 2015, Nature, 518, 512

Yaqoob, T. 2012, ApJ, 754, 8